
Understanding Model Averaging in Federated Learning on Heterogeneous Data

Tailin Zhou¹, Zehong Lin¹, Jun Zhang¹, Danny H.K. Tsang^{2,1}

¹ Hong Kong University of Science and Technology

² Hong Kong University of Science and Technology (Guangzhou)
{tzhouaq, eezhlin, eejzhang, eetsang}@ust.hk

Abstract

Model averaging, a widely adopted technique in federated learning (FL), aggregates multiple client models trained on heterogeneous data to obtain a well-performed global model. However, the rationale behind its success is not well understood. To shed light on this issue, we investigate the geometric properties of model averaging by visualizing the loss/error landscape. The geometrical visualization shows that the client models surround the global model within a common basin, and the global model may deviate from the bottom of the basin even though it performs better than the client models. To further understand this phenomenon, we decompose the expected prediction error of the global model into five factors related to client models. Specifically, we find that the global-model error after early training mainly comes from *i*) the client-model error on non-overlapping data between client datasets and the global dataset and *ii*) the maximal distance between the global and client models. Inspired by these findings, we propose adopting iterative moving averaging (IMA) on global models to reduce the prediction error and limiting client exploration to control the maximal distance at the late training. Our experiments demonstrate that IMA significantly improves the accuracy and training speed of existing FL methods on benchmark datasets with various data heterogeneity.

1 Introduction

Federated learning (FL) [28] enables clients to collaboratively train a machine learning model while keeping their data decentralized to protect privacy. One of the primary challenges in FL is the data heterogeneity across clients, which diverges client models [43]. Nonetheless, the global model obtained by federated model averaging (FMA)¹ has been shown to enable the global model to converge throughout the training process. Specifically, at each round, FMA aggregates K client models updated locally on heterogeneous data to obtain a global model \mathbf{w} as $\mathbf{w} \leftarrow \sum_{k=1}^K (n_k / \sum_k n_k) \mathbf{w}_k$, where \mathbf{w}_k is the k -th client model and n_k is the size of the k -th client dataset. According to [36], FL frequently outperforms the expectation of theoretical analysis, where FMA is thought to play a crucial role [13, 28]. Despite the empirical success of FMA, it is unclear how it mitigates data heterogeneity.

Model averaging, first introduced in [29], is a widely-used technique to reduce communication [27] and variance reduction [42, 12] in distributed/decentralized learning [45, 1, 17] by periodically averaging models trained over parallel workers with homogeneous data. Surprisingly, model averaging also works well empirically when adopted in FL with heterogeneous data (i.e., FMA) [43, 13]. From the perspective of optimization theory, existing works, e.g., [25, 40], analyze the convergence rate of FL with an assumption of bounded gradient dissimilarity (i.e., an upper bound on the distance

¹To distinguish from model averaging in other communities (e.g., distributed learning with homogeneous data), we term model averaging in FL on heterogeneous data as federated model averaging in this work.

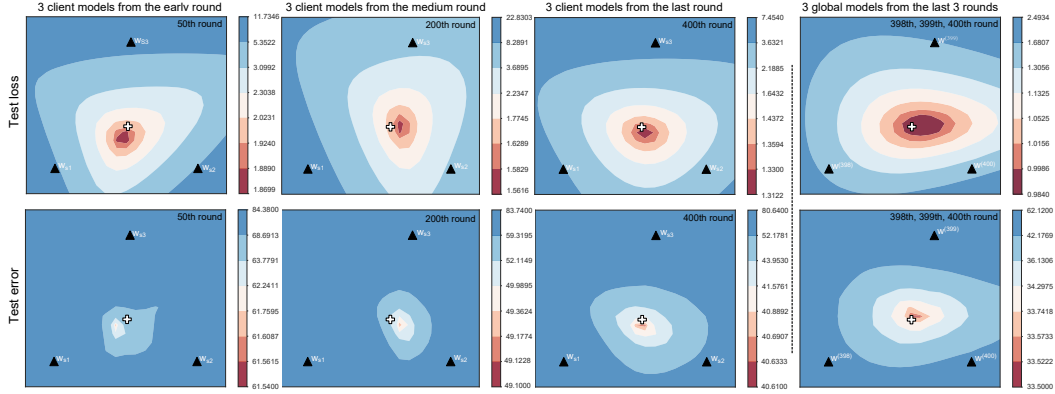


Figure 1: Visualization of the test loss (**top row**) and classification error (**bottom row**) landscapes on the global dataset, along with three client models from the early stage (**first column**), middle stage (**second column**) and final stage (**third column**), as well as the visualization of three global models from the final three rounds (**fourth column**). The *black triangles* represent the location of three models in the plane, while the *white cross* represents the location of their averaged model.

between the global and client gradients), and then use this bound to show how heterogeneous data degrades convergence. However, a recent work [36] finds that the practical average drift of client gradients is significantly smaller than this bound, which indicates that this bound may not characterize the effect of data heterogeneity well. FMA may be responsible for the modest practical average drift, as suggested in [35, 36], but a conclusive explanation of how FMA assists FL is still lacking.

This work first investigates the geometrical properties of FMA by visualizing the loss/error landscape in Section 2. Our investigation reveals that the global model is closely surrounded by client models within a common basin and consistently achieves the lower test loss and error. Then, we decompose the expected prediction error of the global model to establish a connection between the error of the global model and client models in Section 3. Based on this connection, we analyze how the global-model error is impacted by various factors throughout the training process. To mitigate the negative effects of these factors, we employ iterative moving averaging (IMA) on global models along their optimization trajectory, as discussed in Section 4.

Contribution. We aim to unravel the working mechanism of FMA on heterogeneous data by its geometrical properties and error decomposition. Our main contributions are summarized as follows:

- We investigate the dynamics of test loss/classification-error landscapes of global and client models. Through the use of landscape visualization, we observe that the global model is closely surrounded by client models in a common basin, but may deviate from its lowest point, despite having a lower loss/error than client models.
- We decompose the global-model error by using the bias and variance of client-model prediction errors on the global dataset. We demonstrate that, after early training, the global-model error is dominated by the error of client models on non-overlapping data between their datasets and the global dataset, and their maximal distance from the global model.
- To mitigate the error caused by the prediction errors and distance, we employ IMA on global models and decay client exploration in the late training stages. Our experiments show that IMA improves the performance of existing methods on various benchmark datasets.

2 Loss Landscape Visualization of Federated Model Averaging

Problem formulation. We consider an FL framework with K clients, where each client has a dataset $\mathcal{D}_k = \{(x, y)\}$, and the global dataset is denoted by $\mathcal{D} = \cup_{k=1}^K \mathcal{D}_k$. The FL objective is to minimize the expected error $\mathcal{E}(\mathbf{w}) = \mathbb{E}_{(x, y) \in \mathcal{D}} [l(\mathbf{w}; (x, y))] = \sum_{k=1}^K (n_k / \sum_k n_k) \mathbb{E}_{(x, y) \in \mathcal{D}_k} [l_k(\mathbf{w}; (x, y))]$, where $l(\cdot)$ and $l_k(\cdot)$ denote the global and local loss functions, respectively. In this section, we consider the cross-entropy loss and focus on classification

tasks to explore the geometrical properties of FMA. The experiment setup related to Figure 1 involves 100 clients, where each client dataset holds two class shards of CIFAR-10 [18], as used in [28] (see Appendix C.3 for details).

Averaged model enjoys lower test loss and error. As shown in Figure 1, we follow [6, 11] to visualize the dynamics of the test loss and classification error landscapes of three client models randomly sampled from 100 clients, which is tested on the global dataset. Additional visualization results for various setups, including different training datasets, data heterogeneity, models and FL setups, are provided in Appendix A. Notably, we observe that the averaged model (i.e., the *white cross*) of the three client models (i.e., the *black triangles*) is consistently located at the regions with lower test loss and classification error than individual client models. This indicates that FMA prevents client models from over-fitting on client datasets and being aggregated into the global model.

Moreover, we observe a bias between the *white cross* and the lowest loss/error point in the first three columns of Figure 1. To investigate it further, we visualize the loss/error landscape of global models obtained from the final three rounds. The lower loss/error on the averaged model of the three global models (i.e., the *white cross* in the fourth column in Figure 1) reveals that the global model at each round may deviate from the lowest loss point, which will be analyzed in Section 4.

Client modes surround the global mode closely in a common basin. In Figure 1, the second row demonstrates that the test classification errors of client models are about 80%, which represents their lowest classification error when trained locally. This indicates that the client models are close to their local optima, which we term as *client modes* in this work. Meanwhile, Figure 1 illustrates that the averaged model is surrounded by client models and located in the neighborhood of a local optimum of the global model, which we term as the *global mode*. These observations suggest that the global mode is closely surrounded by client modes within a common basin, as further verified by Figure 3.

Geometrically, the test loss/error landscape of FMA may be viewed as a basin, with client modes reaching the wall of the basin and the global mode at the bottom, as shown in Figure 1. This geometric property provides novel insight into the mechanism behind the small averaged drift of client updates [36]: the drift can be limited since the direction of client updates can radiate all around, especially in the late training stage. In Section 3, we will demonstrate the relationship between the error of the global model and client models on the global dataset.

3 Expected Error Decomposition

We define the model function of \mathbf{w} as $f_{\mathbf{w}} : \mathcal{X} \rightarrow \mathcal{Y}$, where \mathcal{X} and \mathcal{Y} are input and output spaces, respectively. Herein, we focus on the mean-square error (MSE) loss for simplicity, i.e., $l(\mathbf{w}; (x, y)) = (y - f_{\mathbf{w}}(x))^2$, which can be extended to other losses [5]. Following [2, 16], given a subspace $\mathcal{W}_{\mathcal{D}_{tr}}$ that contains all solutions trained on \mathcal{D}_{tr} , the bias-variance decomposition on the expected error of a model \mathbf{w} in $\mathcal{W}_{\mathcal{D}_{tr}}$ tested on \mathcal{D}_{te} can be expressed as:

$$\mathbb{E}_{\mathbf{w} \in \mathcal{W}_{\mathcal{D}_{tr}}} \mathcal{E}_{\mathcal{D}_{te}}(\mathbf{w}) = \underbrace{\mathbb{E}_{(x,y) \in \mathcal{D}_{te}} [(y - \bar{f}_{\mathcal{D}_{tr}}(x))^2]}_{\text{Bias}\{f|(x,y)\}} + \underbrace{\mathbb{E}_{\mathbf{w} \in \mathcal{W}_{\mathcal{D}_{tr}}} [(f_{\mathbf{w}}(x) - \bar{f}_{\mathcal{D}_{tr}}(x))^2]}_{\text{Var}\{f|x\}} \quad (1)$$

where $\bar{f}_{\mathcal{D}_{tr}}(\cdot) = \mathbb{E}_{\mathbf{w} \in \mathcal{W}_{\mathcal{D}_{tr}}} [f_{\mathbf{w}}(\cdot)]$ is the expected output of all models in $\mathcal{W}_{\mathcal{D}_{tr}}$ (i.e., the output of model ensemble of $\mathcal{W}_{\mathcal{D}_{tr}}$). Given $\mathcal{W}_{\mathcal{D}_{tr}}$ and a sample $(x, y) \in \mathcal{D}_{te}$, $\text{Bias}\{f|(x,y)\}$ denotes the bias between the ground truth y and the ensemble output $\bar{f}_{\mathcal{D}_{tr}}(x)$, and $\text{Var}\{f|x\}$ denotes the expected MSE between $f_{\mathbf{w}}(x)$ and $\bar{f}_{\mathcal{D}_{tr}}(x)$, which depends on the discrepancy between \mathcal{D}_{tr} and \mathcal{D}_{te} [31, 39].

Connecting FMA to the weighted model ensemble (WENS). To incorporate model averaging into (1), we analyze the relationship between FMA and WENS in FL by adapting [11], which yields:

Lemma 1. (FMA and WENS. Proof in Appendix D.1) Given K models $\{\mathbf{w}_k\}_{k=1}^K$ and $n_i/n_j \neq \infty$ when $i \neq j$, we denote $n = \sum_k n_k$, $\Delta_k = \max_k \|\mathbf{w}_k - \mathbf{w}_{\text{FMA}}\|$ and $\Delta = \max_k \Delta_k$ and have:

$$f_{\text{WENS}}(x) - f_{\mathbf{w}_{\text{FMA}}}(x) = \left\langle \Delta f_{\mathbf{w}_{\text{FMA}}}(x), \sum_{k=1}^K \frac{n_k}{n} \Delta_k \right\rangle + O(\Delta^2) = O(\Delta^2) \quad (2)$$

where $f_{\text{WENS}}(\cdot) = \sum_{k=1}^K \frac{n_k}{n} f_{\mathbf{w}_k}(\cdot)$ denotes the WENS on K models.

Lemma 1 shows that the global model function $f_{\text{FMA}}(\cdot)$ is a first-order approximation of the WENS function $f_{\text{WENS}}(\cdot)$ of the client models when Δ is small, as verified in Figure 3.

Theoretical error decomposition of the FMA model. We apply Lemma 1 to adapt the bias-variance decomposition (1) to the FL version. Specifically, the model \mathbf{w} in (1) is substituted by K client models $\{\mathbf{w}_k\}_{k=1}^K$, and \mathcal{D}_{tr} and \mathcal{D}_{te} is adapted as client datasets $\{\mathcal{D}_k\}_{k=1}^K$ and the global dataset \mathcal{D} , respectively. Meanwhile, $\bar{f}_{\mathcal{D}_{\text{tr}}}(\cdot) = \mathbb{E}_{\{\mathbf{w}_k\}_{k=1}^K \in \prod_k \mathcal{W}_{\mathcal{D}_k}} [f_{\{\mathbf{w}_k\}_{k=1}^K}(\cdot)] = \mathbb{E}_{\{\mathbf{w}_k\}_{k=1}^K} [f_{\text{WENS}}(\cdot)]$ denotes the ensemble output of the combination subspace on K client models. Then, we decompose the expected error of $f_{\text{FMA}}(\cdot)$ tested on \mathcal{D} as:

Theorem 1. (Global-model error decomposition. Proof in Appendix D.2) Given K client models $\{\mathbf{w}_k\}_{k=1}^K \in \prod_k \mathcal{W}_{\mathcal{D}_k}$, the expected error of the FMA’s model \mathbf{w}_{FMA} on \mathcal{D} is decomposed as:

$$\begin{aligned} \mathbb{E}_{\{\mathbf{w}_k\}_{k=1}^K} \mathcal{E}(\mathbf{w}_{\text{FMA}}) &= \frac{1}{n} \sum_{(x,y) \in \mathcal{D}} \left[\sum_{k=1}^K \frac{n_k}{n} \text{TrainBias}\{f_{\mathbf{w}_k}|(x,y)\} + \frac{n_k}{n} \text{HeterBias}\{f_{\mathbf{w}_k}|(x,y)\} \right]^2 \\ &\quad + \sum_{k=1}^K \frac{n_k^2}{n^2} \text{Var}\{f_{\mathbf{w}_k}|x\} + \sum_k \sum_{k' \neq k} \frac{n_k n_{k'}}{n^2} \text{Cov}\{f_{\mathbf{w}_k}, f_{\mathbf{w}_{k'}}|x\} + O(\Delta^2) \end{aligned} \quad (3)$$

where $\text{TrainBias}\{f_{\mathbf{w}_k}|(x,y)\} = \mathbb{I}[(x,y) \in \mathcal{D}_k] (y - \mathbb{E}_{\mathbf{w}_k}[f_{\mathbf{w}_k}(x)])$; $\text{HeterBias}\{f_{\mathbf{w}_k}|(x,y)\} = \mathbb{I}[(x,y) \in \mathcal{D} \setminus \mathcal{D}_k] (y - \mathbb{E}_{\mathbf{w}_k}[f_{\mathbf{w}_k}(x)])$; $\text{Var}\{f_{\mathbf{w}_k}|x\} = \mathbb{E}_{\mathbf{w}_k} \left[(f_{\mathbf{w}_k}(x) - \mathbb{E}_{\mathbf{w}_k}[f_{\mathbf{w}_k}(x)])^2 \right]$; $\text{Cov}\{f_{\mathbf{w}_k}, f_{\mathbf{w}_{k'}}|x\} = \mathbb{E}_{\mathbf{w}_k, \mathbf{w}_{k'}} \left[(f_{\mathbf{w}_k}(x) - \mathbb{E}_{\mathbf{w}_k}[f_{\mathbf{w}_k}(x)]) (f_{\mathbf{w}_{k'}}(x) - \mathbb{E}_{\mathbf{w}_{k'}}[f_{\mathbf{w}_{k'}}(x)]) \right]$.

The meanings of the five factors in Theorem 1 are as follows: *i*) $\text{TrainBias}\{f_{\mathbf{w}_k}|(x,y)\}$ denotes the $\text{Bias}\{f|(x,y)\}$ term in (1) when given a client model \mathbf{w}_k trained on \mathcal{D}_k and a sample $(x,y) \in \mathcal{D}_k$; *ii*) $\text{HeterBias}\{f_{\mathbf{w}_k}|(x,y)\}$ denotes the $\text{Bias}\{f|(x,y)\}$ when given \mathbf{w}_k and a non-overlapping sample (x,y) between \mathcal{D} and \mathcal{D}_k (i.e., $(x,y) \in \mathcal{D} \setminus \mathcal{D}_k$); *iii*) $\text{Var}\{f_{\mathbf{w}_k}|x\}$ denotes the $\text{Var}\{f|x\}$ term in (1) when given \mathbf{w}_k and a sample (x,y) , which does not depend on y ; *iv*) $\text{Cov}\{f_{\mathbf{w}_k}, f_{\mathbf{w}_{k'}}|x\}$ denotes the output correlation of \mathbf{w}_k and $\mathbf{w}_{k'}$ given the same data sample (x,y) , which does not depend on y ; *v*) $O(\Delta^2)$, referred to the locality in [11, 31], denotes the maximum distance between client models and the global model. Next, we adapt Theorem 1 to provide an upper bound for the global-model error.

Corollary 1. (An upper bound of the global-model error. Proof in Appendix D.3) Comparing the error of the global model with client models, we have $\mathbb{E}_{\{\mathbf{w}_k\}_{k=1}^K} \mathcal{E}(\mathbf{w}_{\text{FMA}}) \leq \max_k \mathbb{E}_{\mathbf{w}_k} \mathcal{E}(\mathbf{w}_k)$ when $\Delta = \|\Delta_k\|$, where the equality holds when K client models $\{\mathbf{w}_k\}$ are identically distributed.

In the following, we discuss the effects of the five terms of Theorem 1 on FMA in detail.

Heterogeneous bias dominates the global-model error after the early training. Figure 2 shows that the $\text{TrainBias}\{f_{\mathbf{w}_k}|(x,y)\}$ is effectively reduced to almost zero, which is because the number of local updates is sufficient for client models to fit their own datasets. Meanwhile, $\text{HeterBias}\{f_{\mathbf{w}_k}|(x,y)\}$ arises from data heterogeneity, which makes it difficult for clients to address it through local training. However, due to the geometric property observed in Section 2, FMA provides an initialization point with enriched global information (closer to the global mode than client modes) for client models to mitigate this bias.

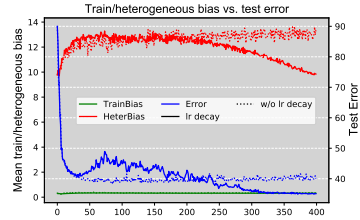


Figure 2: Bias terms w.r.t rounds.

Moreover, the larger the local update step, the more global information provided by the FMA is forgotten, and the greater the heterogeneous bias, due to the catastrophic forgetting phenomenon in neural networks [7, 15]. This is validated by the cases with and without learning rate (lr) decay in Figure 2. We use a round-exponential decay lr to control the update size, which is a straightforward approach to preventing the catastrophic forgetting in FL [32]. In the early phase, heterogeneous bias does not have a significant impact on the test error because the error continues to decrease even if the bias increases. However, thereafter, both the error and the bias show a positive correlation in both cases. For example, after approximately 40 rounds, they both increase and then decrease in the case of lr decay, and the error grows slightly with the bias in the case without lr decay.

Controlling the locality helps reduce the global-model error at the late training. We take the L2 distance to measure the locality term in Figure 3. Theorem 1 demonstrates that the test error decreases as the maximum distance between client models and the global model, i.e., Δ , reduces. Figure 3 shows that the locality is larger in the case without lr decay, which results in a more significant test error. Before the 40th round, the test errors of both cases continue to decline even if an increase of the locality occurs within this period. Then, the case of lr decay shows that the locality reduces while the error goes up between 40 to 75 rounds. This indicates that the locality does not have a strong correlation with the error at the early training. Additionally, the locality stabilizes after the early training (i.e., the locality has an upper bound in both cases). This further verifies the proximity of client modes to the global mode, as indicated in Section 2.

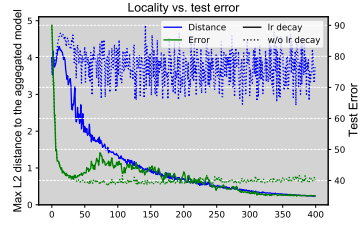


Figure 3: Locality w.r.t rounds.

FMA with more client models to be aggregated diminishes the whole variance term. See more theoretical analysis in Appendix B.1 due to the page space limitation. In FMA, $\mathbb{E}_{(x,y) \in \mathcal{D}}[\text{Var}\{f_{\mathbf{w}_k}|x\}]$ can be viewed as a constant V_k since $\text{Var}\{f_{\mathbf{w}_k}|x\}$ depends

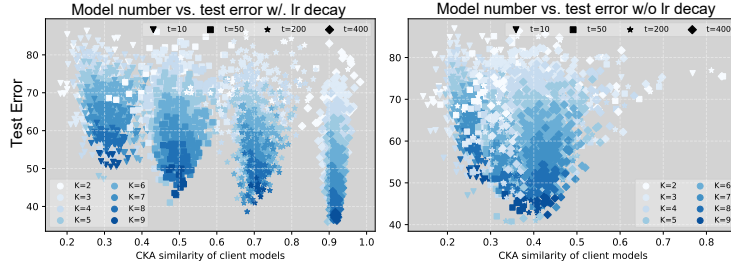


Figure 4: Test error w.r.t model number and model similarity.

on the discrepancy between \mathcal{D} and \mathcal{D}_k , as shown in (1). Suppose $\max_k \{V_k\} \leq \epsilon$. Then, the whole variance term in (3) is $\sum_k n_k^2/n^2 V_k$ and it is upper bounded by $\epsilon \sum_{k=1}^K n_k^2/n^2$. Therefore, FMA can keep this upper bound diminishing by averaging more client models (i.e., larger K induces smaller $\sum_{k=1}^K n_k^2/n^2$) to reduce the global-model error when ϵ is tight for $\max_k \{V_k\}$. Figure 4 verifies this effect on FMA at the whole training, while it weakens with the increase of the model number.

Meanwhile, we take the CKA similarity [18] that computes the output correlation across client models given the same input to measure the covariance term. As shown in Figure 4, data heterogeneity causes the covariance term to be inherently small, especially in the case without lr decay. That is, maintaining client models more diverse (e.g., [20, 31]) may not have much of an effect on reducing the global-model error, and even hurt the performance at the late training stage, as suggested by the comparison between both cases at the 400th round in Figure 4. On the other hand, we show that the covariance term is small but it has a lower bound in Appendix B.2, which depends on the maximum discrepancy across client datasets. The lower bound implies that this effect of FMA in reducing the global-model error by controlling the diversity of client models is limited.

Summary. *i)* $\text{TrainBias}\{f_{\mathbf{w}_k}|(x, y)\}$ keeps almost zero during the whole training; *ii)* $\text{HeterBias}\{f_{\mathbf{w}_k}|(x, y)\}$ and $O(\Delta^2)$ dominate the FMA-model test error after the early training; *iii)* the whole term of $\text{Var}\{f_{\mathbf{w}_k}|x\}$ can be reduced with larger model number; *iv)* $\text{Cov}\{f_{\mathbf{w}_k}, \mathbf{w}_k|x\}$ is too small to affect on the FMA-model error. Therefore, besides aggregating more client models, controlling $\text{HeterBias}\{f_{\mathbf{w}_k}|(x, y)\}$ and $O(\Delta^2)$ after the early training can reduce the global-model error in FL.

4 Proposed Method: Federated Iterative Model Averaging

Analysis of the deviation of global models. Theorem 1 provides a novel understanding of how the participation rate and weighted averaging lead to this deviation. Specifically, the participation rate may cause the one-cohort dataset of participating clients $\mathcal{D}_C = \cup_{i=1}^C \mathcal{D}_i$ to deviate from \mathcal{D} , while the weighted averaging may assign more weight to clients with datasets that are large but imbalanced from \mathcal{D} , which amplifies the deviation from \mathcal{D}_C to \mathcal{D} . Then, $\text{HeterBias}\{f_{\mathbf{w}_i}|(x, y)\}$ in Theorem 1 cannot be fully reduced since one-cohort client models $\{\mathbf{w}_i\}_i^C$ suffer from the data $(x, y) \in \mathcal{D} \setminus \mathcal{D}_C$. Consequently, we observe the deviation of global models from the lowest point in Figure 1.

Moreover, we find that lower loss/error points consistently exist within the interpolation of two global models from different rounds, as depicted in Figure 5(b). This observation suggests that interpolated

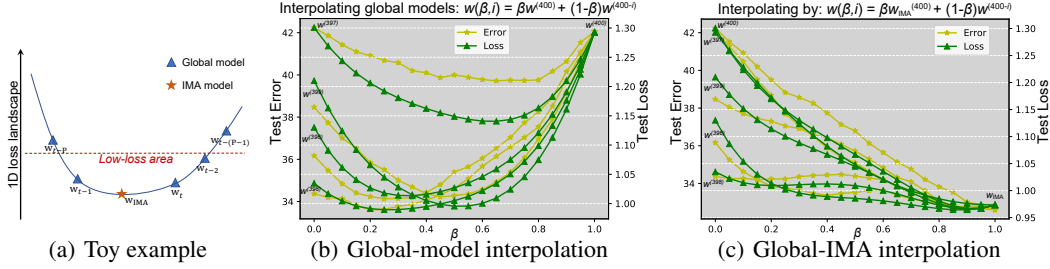


Figure 5: (a) a toy example of IMA; (b) interpolation among global models to validate their deviation; (c) interpolation between the IMA and global models to indicate the flatness of the IMA model.

models keep more global information than global models while keeping within a common basin. Therefore, we apply Theorem 1 to the geometric properties of FMA to alleviate the deviation.

Iterative moving averaging (IMA). The missing information of one-cohort client models on $(x, y) \in \mathcal{D} \setminus \mathcal{D}_C$ can be compensated by utilizing historical global models. The compensation can be achieved by aggregating historical global models into the latest one, as supported in Figure 5(b). Therefore, we propose using IMA on historical global models after sufficient training rounds, instead of ignoring them in conventional FMA. Specifically, as illustrated in Figure 5(a), after t_s rounds, the server performs FMA with IMA to obtain an averaged model from a time window of previous rounds:

$$\mathbf{w}_{\text{IMA}}^{(t)} \leftarrow \frac{1}{P} \sum_{i=0}^{P-1} \mathbf{w}^{(t-i)}, \quad t \geq t_s, \quad (4)$$

where $\mathbf{w}_{\text{IMA}}^{(t)}$ is the IMA model of the t -th round, P is the size of the time window, and t_s is the starting round of IMA. To reduce the impact of information noise brought by historical global models, we initiate IMA in the later training phase, such as $0.75R$ with R denoting the total training rounds. Importantly, IMA only requires storing P global models $\{\mathbf{w}^{(\tau)}\}_{\tau=t-P}^t$ obtained by FMA and initializing client models with $\mathbf{w}_{\text{IMA}}^{(t)}$ in the next round, without modifying client participation or weighted aggregation. As such, IMA can be readily integrated into various FL methods to keep the global model within the low-loss/error region, as demonstrated in Figures 5(c) and 7(c).

Mild client exploration in IMA. Theorem 1 indicates that controlling the locality can reduce the global-model error during late-stage training. Based on this insight and the geometric properties in Section 2, we highlight that it is crucial to control the magnitude of client updates once the global model enters the low-loss area after sufficient training rounds, as illustrated in Figure 5(a). Otherwise, it may result in clients reaching their local modes since client modes are close to the global mode, such that the global model deviates from the low-loss area. To this end, we adopt a more aggressive lr decay for IMA to control client updates (i.e., a significant exponential decay, such as 0.03 lr decay per round). Table 3 demonstrates that some methods, such as a small and constant lr in IMA, yield similar results to ours provided that they can sufficiently constrain client updates.

5 Experiments

Data heterogeneity. We examine label/feature distribution skew in data heterogeneity [13] and refer to them as label/feature skew. To create label skew, we divide FMNIST [38] and CIFAR-10/100 into *data shards with the same sample number* for clients (e.g., $\#C = 2$ denotes that each client holds two classes as [28]). We use the Dirichlet distribution $Dir(\alpha)$ to create client datasets with *different sample numbers* according to [41]. Moreover, we combine label skew and feature skew on Digit Fives [26] and PACS [21]. Specifically, we divide each domain dataset (i.e., feature skew) of them into 20 subsets, each for one client, with various label distributions (i.e., label skew).

Datasets and models. We evaluate the performance of baselines with and without IMA on different models and datasets under both label and feature skews. The mean accuracy of the global model for the last 10 rounds (mean top-1 accuracy of all domains in Digit Five and PACS) is reported in Table 1. For label skew, we train CNN models [28] on FMNIST and CIFAR-10, and train ResNet18 [9] and

Table 1: Mean top-1 last-10-round accuracy comparison of all methods with and without IMA under label skew (including $\#C = 2$ and $\alpha = 0.1$) and feature skew (FS). We follow [32] to use Pachinko Allocation (PA) [24] to create a federated CIFAR-100. Bold text indicates the best results between IMA and IMA-free methods, while underline text denotes the best results with or without IMA.

Dataset (Model)	Heter Data	FedAvg (+IMA)	FedProx (+IMA)	FedASAM (+IMA)	FedFA (+IMA)	FedNova (+IMA)	FedAdam (+IMA)	FedYogi (+IMA)	FedGMA (+IMA)
FMNIST (CNN)	$\#C = 2$	81.17(84.68)	79.78(83.77)	84.69(85.01)	<u>85.60(88.06)</u>	81.23(84.65)	83.53(86.99)	82.42(86.86)	80.89(84.56)
	$\alpha = 0.1$	80.13(83.06)	78.76(81.64)	80.81(82.88)	<u>82.97(86.45)</u>	79.98(83.15)	78.85(83.54)	79.66(83.95)	80.18(83.14)
CIFAR-10 (CNN)	$\#C = 2$	62.34(67.37)	61.71(67.03)	62.60(63.64)	<u>67.49(69.19)</u>	62.34(67.46)	64.49(69.59)	66.68(68.74)	62.25(67.47)
	$\alpha = 0.1$	61.00(64.57)	61.31(64.80)	56.92(59.10)	<u>64.99(67.03)</u>	55.11(60.09)	61.61(66.25)	64.12(65.86)	61.18(64.36)
CIFAR-10 (Resnet)	$\#C = 2$	50.10(59.64)	53.98(61.65)	49.01(56.78)	<u>46.56(56.15)</u>	49.65(59.30)	54.04(59.05)	<u>54.45(59.73)</u>	49.42(58.79)
	$\alpha = 0.1$	49.96(56.37)	<u>52.13(55.07)</u>	48.96(54.41)	42.84(48.88)	33.72(40.52)	47.47(47.60)	50.92(51.26)	49.89(55.93)
CIFAR-100 (VGG)	$\alpha = 0.1$ (+PA)	38.99(39.89)	38.88(39.93)	37.51(38.25)	<u>43.47(44.68)</u>	39.21(39.96)	38.96(39.83)	38.89(39.29)	39.30(40.02)
CIFAR-100 (Resnet)	$\alpha = 0.1$ (+PA)	31.60(32.97)	32.06(33.27)	28.35(29.34)	31.24(34.03)	32.01(33.50)	<u>37.87(40.93)</u>	37.55(40.27)	31.65(32.90)
Digit Five (CNN)	$\#C = 2$ (+FS)	87.90(90.15)	88.14(90.04)	88.68(89.97)	<u>90.26(91.16)</u>	87.77(89.53)	85.63(91.50)	86.31(91.25)	87.91(90.33)
	$\alpha = 0.1$ (+FS)	90.45(91.38)	90.52(91.48)	90.53(91.41)	<u>90.57(91.58)</u>	90.10(90.76)	90.55(92.20)	<u>91.06(92.30)</u>	90.50(91.49)
PACS (Alexnet)	$\#C = 2$ (+FS)	57.47(58.01)	60.88(61.51)	61.15(61.46)	56.57(57.36)	60.24(63.53)	54.63(60.09)	55.54(57.03)	57.33(62.17)
	$\alpha = 0.1$ (+FS)	40.36(47.36)	<u>42.15(49.13)</u>	39.57(43.29)	41.95(47.12)	13.96(16.10)	33.76(43.23)	39.97(40.56)	41.73(47.46)

VGG11 [33] on CIFAR-10/100. For label-feature skew, we train CNN on Digit Fives and Alexnet [19] on PACS. We replace BN layers with GN layers following [10].

Experimental setup and baselines. (see Tables 5 and 7 for more details) In the FL setup, unless otherwise specified, we use a batch size and of 50 and 5 local epochs, with 100 clients participating in FL for 400 rounds, where one-tenth of the clients participate in each round. For client optimizers, we follow a standard configuration from the FL benchmark [22], and use the SGD optimizer with a learning rate (lr) of 0.01 and 0.9 momentum. For baselines, in addition to FedAvg [28], we include other methods that improve FedAvg based on the client side, such as parameter-regularization: FedProx [23], flatness-improvement: FedASAM [3] and feature-classifier-alignment: FedFA [44]) and the server side, such as update-normalization: FedNova [37], server-momentum: FedADAM/FedYogi [32] and gradient-masking: FedGMA [34]. Note that our IMA does not conflict with these methods.

Performance on label skew. Table 1 illustrates that, for label skew (i.e., $\#C = 2$ and $\alpha = 0.1$), IMA enhances the performance of all methods on different datasets and models. Across all datasets (FMNIST, CIFAR-10, and CIFAR-100), adding IMA consistently improves performance. For instance, when training with a CNN model on FMNIST, FedFA with IMA achieves the highest accuracy of 88.06% among baselines, compared with 79.7% for FedProx without IMA. The most significant improvement is achieved by IMA when training ResNet on CIFAR-10, where the performance rises from 49.65% to 59.30%, i.e., a gain of 9.65%. However, as shown in Table 1, the benefits of IMA depend on the heterogeneity level of label skew, with greater heterogeneity resulting in more significant performance gains. For example, the maximum performance gain for CIFAR-10 with label skew $\alpha = 0.1$ is 6.42% (FedAvg with ResNet) compared with 3.06% for CIFAR-100 with $\alpha = 0.1$ and Pachinko Allocation [24], which is milder than $\alpha = 0.1$.

Performance on label-feature skew and different α of label skew. To further investigate the effect of data heterogeneity on IMA, we conduct tests on Digit Five and PACS datasets under both label and feature skew. Our findings on feature skew, as shown in Table 1, are similar to those observed in the cases of label skew. For instance, we observe a greater performance gain with IMA on PACS than Digit Five due to the more severe heterogeneity of feature skew in PACS with $\alpha = 0.1$. To validate these findings, we test different levels of label skew on CIFAR-10 and plot the results in Figure 6(a). The figure shows that IMA under smaller α (i.e., more heterogeneous) achieves greater performance gains; e.g., the IMA gain of $\alpha = 0.05$ is larger than 5% for all baselines, compared with the insignificant gain of $\alpha = 0.8$. Therefore, Table 1 and Figure 6(a) demonstrate IMA’s effectiveness in mitigating the negative effect of data heterogeneity, especially under extreme heterogeneity.

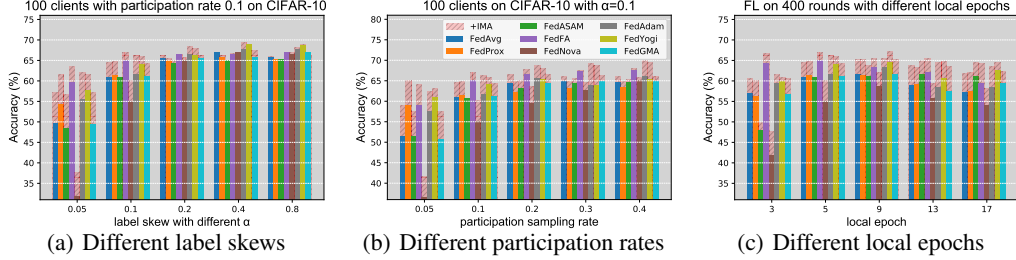


Figure 6: Performance of all methods with and without IMA on different federated setups.

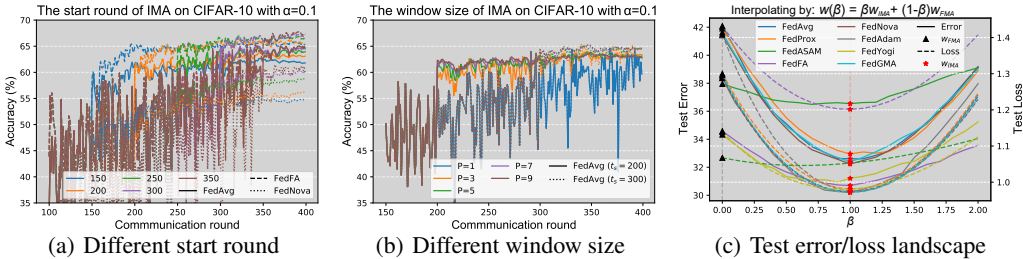


Figure 7: Ablation studies on IMA and landscape visualization between FMA and IMA models.

Reduction in communication overhead. Table 2 presents the communication efficiency of IMA with different starting rounds to achieve a targeted accuracy on CIFAR-10 with $\alpha = 0.1$, where FedASAM and FedNova are not reported because their performance is worse than the targeted accuracy. The results illustrate that IMA can significantly reduce the communication overhead when started at earlier rounds, compared with three quarters of the total rounds used in Table 1; e.g., starting IMA at the 150th round saves communication by nearly half-up for FedAdam and FedProx.

Table 2: Required rounds by IMA with different start rounds t_s when the accuracy reaches 61.61% from Table 1.

(+IMA) t_s	150	200	250	300	FMA
FedAvg	318($\times 1.24$)	257($\times 1.53$)	260($\times 1.51$)	309($\times 1.28$)	394($\times 1$)
FedProx	201($\times 1.96$)	210 ($\times 1.88$)	260($\times 1.52$)	309($\times 1.28$)	394($\times 1$)
FedFA	183 ($\times 1.87$)	212($\times 1.61$)	258($\times 1.32$)	308($\times 1.11$)	341($\times 1$)
FedAdam	193($\times 2.03$)	210 ($\times 1.87$)	259($\times 1.51$)	306 ($\times 1.28$)	392($\times 1$)
FedYogi	195($\times 1.85$)	210 ($\times 1.71$)	257 ($\times 1.40$)	306 ($\times 1.18$)	360($\times 1$)
FedGMA	316($\times 1.25$)	242($\times 1.63$)	260($\times 1.52$)	309($\times 1.28$)	394($\times 1$)

Performance on different client participation rates. We evaluate the performance of IMA with participation rates ranging from 0.05 to 0.4 in Figure 6(b), in addition to the results obtained with a 0.1 participation rate presented in Table 1. The figure indicates that the gain achieved by IMA generally increases as the client participation rate decreases. For example, the gain observed with a 0.05 participation rate is approximately twice that of a 0.2 participation rate, at around 5%. Furthermore, Figure 6(b) also verified the global-model deviation induced by low participation rates highlighted in Section 4. It illustrates that smaller participation rates, lead to larger deviations between the client-cohort and the global datasets, thereby amplifying the negative effects of data heterogeneity.

Performance on different local epochs. To assess the robustness of IMA, we evaluate its performance on different local epoch settings ranging from 3 to 17, as shown in Figure 6(c). The results show that IMA consistently improves all baseline methods across different epoches. Notably, we also observe that the performance gain remains stable even when the number of local epochs increases. This is because client modes are closely located around the global mode within the same basin due to FMA, as observed in Section 2. That is, the advantages of IMA continue to apply even when client models are close to their local optima, since IMA may close global models to the global mode.

Ablation on starting rounds and window size of IMA. The results in Table 2 indicate that starting IMA at a later round requires more communication overhead. However, Figure 7(a) shows that starting IMA at the 350th round leads to the best final performance in terms of accuracy compared with other methods. This finding demonstrates a trade-off between communication efficiency and performance in IMA. Moreover, increasing the window size improves the training stability but can hurt the final accuracy if IMA starts early, as seen in FedAvg with $t_s = 200$ and $P = 9$ achieving lower accuracy than other cases in Figure 7(b)).

Table 3: Accuracy v.s. decay schemes.

IMA w/ decay	Exp Decay	Const LR	Cyclic Decay	Epoch Decay	NA Decay
FedAvg	64.57	64.50	64.27	62.96	63.96
FedProx	64.80	64.73	64.59	63.14	64.12
FedASAM	59.10	58.14	59.33	57.48	58.95
FedFA	67.03	66.62	66.94	66.63	66.40
FedNova	60.09	59.86	59.38	59.04	58.90
FedAdam	66.25	65.89	66.06	64.00	65.62
FedYogi	65.86	65.53	65.51	63.13	65.12
FedGMA	64.36	64.41	64.12	62.97	63.75

Ablation on mild client exploration in IMA. As stated in Section 4, we adopt a more aggressive exponential lr decay per round in IMA than in FMA to restrict client exploration. To explore the necessity of mild client exploration, we conduct experiments on CIFAR-10 with $\alpha = 0.1$ to ablate IMA with different decay schemes, including a tiny constant lr (i.e., lr is 5×10^{-5} in IMA), cyclic lr decay [11] (i.e., decaying lr from 1×10^{-2} to 5×10^{-5} every 20

rounds), epoch decay [30] (i.e., decaying one local epoch per 20 rounds) and non-additional decay (NA) than FMA, as shown in Table 3. Specifically, more aggressive decay schemes that sufficiently constrain client updates (e.g., exponential lr decay or small constant lr) present better performance than milder decay schemes. For instance, exponential decay achieves 64.57% on FedAvg, compared with 62.96% of epoch decay.

Test error/loss landscape between FMA and IMA models. Figure 7(c) depicts the interpolation model between FMA models and IMA models (both from the final round), to show the landscape of test error and test loss. The figure shows that the IMA models reach almost the center (i.e., the lowest point) of both the test error and test loss basins of all baselines, which effectively alleviates the deviation mentioned in Section 4. In contrast, the FMA models only reach the wall of the basin, which verifies the deviation found in Section 2. Moreover, Figure 7(c) shows that these methods reach various basins with different curvature, but it is not true that the flatter the basin, the lower the error (e.g., the basin of FedASAM is flattest, but the error is largest).

6 Related Works

Convergence analysis. Existing works [25, 40, 23, 14, 37] mainly focus on analyzing the convergence of FedAvg and its variants under heterogeneous data based on the bounded-gradient assumption, with a unified framework of convergence analysis presented in [37]. However, a recent work [36] argues that the key assumption is overly pessimistic and neglects the much smaller practical average drift of client updates at optimum, making it difficult to characterize the data heterogeneity. The rationale behind this observation remains unclear, and FMA may serve as a weight-regularization strategy to keep the drift nearly zero under heterogeneous data, as suggested in [35].

Loss landscape, flatness and model diversity. Another common way to explore model performance is loss landscape analysis along the training trajectory. Stochastic weight averaging [11] achieves better generalization by reaching the flat points in the loss basin with cumulatively averaging models along the SGD trajectory. This approach has been extended to distributed learning in [8] and seeks the flatness of domain generalization in [4]. Previous work in distributed learning [42] notes that model averaging may bring client models to a common basin of attraction but does not provide further analysis or visualization. Moreover, keeping models with mild diversity in the model ensemble and model average [20, 31] can improve the generalization of the averaged model. However, the geometric properties of model averaging have not been extensively discussed in previous work [13]. Therefore, to uncover the mechanism behind FMA, we take the first step in understanding the geometrical property of FMA on data heterogeneity by visualizing the loss/error landscape.

7 Discussions and Limitations

This work advances the understanding of how FMA operates in the presence of data heterogeneity and proposes to employ IMA to enhance its performance. Firstly, we investigate the dynamics of the loss landscape of FMA during training and observe that client modes closely surround the global mode within the same basin. Using test error decomposition, we illustrate the relationship between the global model and client models, demonstrating that the heterogeneous bias and locality of the client models dominate the error of the global model after the early training stage. These findings motivate us to adopt IMA on global models at the late training stage, rather than disregarding them in FMA. Our experiments show that IMA significantly improves the accuracy and communication efficiency of existing FL methods under both label and feature skews.

Although we demonstrate the relationship between the global-model and client-model error based on expected error decomposition in Section 3, it is still not clear how to quantify the relationship explicitly in general cases. Future works should analyze how each of five factors dominates the error in the whole training stage. Our proposed IMA can be considered as an FL variant with iterative averaging [12] that averages the final few iterates of the model in the least square regression. Although IMA reaches almost the center of the reached loss basin, it cannot find a better basin with lower loss.

In future work, an IMA variant with an adaptive starting round is deserved to be investigated due to the promising results in Table 2, which can save communication without compromising generalization. Moreover, using more flexible regularization between the global model and client models (e.g., elastic weight consolidation [15]) can further reduce the bias and locality in Theorem 1. We hope that our study can serve as a valuable reference for further analyzing and improving FL.

References

- [1] T. Ben-Nun and T. Hoefler. Demystifying parallel and distributed deep learning: An in-depth concurrency analysis. *ACM Computing Surveys (CSUR)*, 52(4):1–43, 2019.
- [2] G. Brown, J. Wyatt, and P. Sun. Between two extremes: Examining decompositions of the ensemble objective function. In *Multiple Classifier Systems: 6th International Workshop, MCS 2005, Seaside, CA, USA, June 13-15, 2005. Proceedings 6*, pages 296–305. Springer, 2005.
- [3] D. Caldarola, B. Caputo, and M. Ciccone. Improving generalization in federated learning by seeking flat minima. In *Computer Vision–ECCV 2022: 17th European Conference, Tel Aviv, Israel, October 23–27, 2022, Proceedings, Part XXIII*, pages 654–672. Springer, 2022.
- [4] J. Cha, S. Chun, K. Lee, H.-C. Cho, S. Park, Y. Lee, and S. Park. Swad: Domain generalization by seeking flat minima. *Advances in Neural Information Processing Systems*, 34:22405–22418, 2021.
- [5] P. Domingos. A unified bias-variance decomposition. In *Proceedings of 17th International Conference on Machine Learning*, pages 231–238. Morgan Kaufmann Stanford, 2000.
- [6] T. Garipov, P. Izmailov, D. Podoprikin, D. P. Vetrov, and A. G. Wilson. Loss surfaces, mode connectivity, and fast ensembling of dnns. *Advances in Neural Information Processing Systems*, 31, 2018.
- [7] I. J. Goodfellow, M. Mirza, D. Xiao, A. Courville, and Y. Bengio. An empirical investigation of catastrophic forgetting in gradient-based neural networks. *arXiv preprint arXiv:1312.6211*, 2013.
- [8] V. Gupta, S. A. Serrano, and D. DeCoste. Stochastic weight averaging in parallel: Large-batch training that generalizes well. *arXiv preprint arXiv:2001.02312*, 2020.
- [9] K. He, X. Zhang, S. Ren, and J. Sun. Deep residual learning for image recognition. In *Proceedings of the IEEE Conference on Computer Vision and Pattern Recognition*, pages 770–778, 2016.
- [10] K. Hsieh, A. Phanishayee, O. Mutlu, and P. Gibbons. The non-iid data quagmire of decentralized machine learning. In *International Conference on Machine Learning*, pages 4387–4398. PMLR, 2020.
- [11] P. Izmailov, D. Podoprikin, T. Garipov, D. Vetrov, and A. G. Wilson. Averaging weights leads to wider optima and better generalization. *arXiv preprint arXiv:1803.05407*, 2018.
- [12] P. Jain, S. Kakade, R. Kidambi, P. Netrapalli, and A. Sidford. Parallelizing stochastic gradient descent for least squares regression: mini-batching, averaging, and model misspecification. *Journal of Machine Learning Research*, 18, 2018.
- [13] P. Kairouz, H. B. McMahan, B. Avent, A. Bellet, M. Bennis, A. N. Bhagoji, K. Bonawitz, Z. Charles, G. Cormode, R. Cummings, et al. Advances and open problems in federated learning. *Foundations and Trends® in Machine Learning*, 14(1–2):1–210, 2021.

- [14] S. P. Karimireddy, S. Kale, M. Mohri, S. Reddi, S. Stich, and A. T. Suresh. Scaffold: Stochastic controlled averaging for federated learning. In *International Conference on Machine Learning*, pages 5132–5143. PMLR, 2020.
- [15] J. Kirkpatrick, R. Pascanu, N. Rabinowitz, J. Veness, G. Desjardins, A. A. Rusu, K. Milan, J. Quan, T. Ramalho, A. Grabska-Barwinska, et al. Overcoming catastrophic forgetting in neural networks. *Proceedings of the National Academy of Sciences*, 114(13):3521–3526, 2017.
- [16] R. Kohavi, D. H. Wolpert, et al. Bias plus variance decomposition for zero-one loss functions. In *International Conference on Machine Learning*, volume 96, pages 275–83. Citeseer, 1996.
- [17] A. Koloskova, N. Loizou, S. Boreiri, M. Jaggi, and S. Stich. A unified theory of decentralized sgd with changing topology and local updates. In *International Conference on Machine Learning*, pages 5381–5393. PMLR, 2020.
- [18] A. Krizhevsky, G. Hinton, et al. Learning multiple layers of features from tiny images. 2009.
- [19] A. Krizhevsky, I. Sutskever, and G. E. Hinton. Imagenet classification with deep convolutional neural networks. *Communications of the ACM*, 60(6):84–90, 2017.
- [20] S. Lee, S. Purushwalkam Shiva Prakash, M. Cogswell, V. Ranjan, D. Crandall, and D. Batra. Stochastic multiple choice learning for training diverse deep ensembles. *Advances in Neural Information Processing Systems*, 29, 2016.
- [21] D. Li, Y. Yang, Y.-Z. Song, and T. M. Hospedales. Deeper, broader and artier domain generalization. In *Proceedings of the IEEE International Conference on Computer Vision*, pages 5542–5550, 2017.
- [22] Q. Li, Y. Diao, Q. Chen, and B. He. Federated learning on non-iid data silos: An experimental study. *arXiv preprint arXiv:2102.02079*, 2021.
- [23] T. Li, A. K. Sahu, M. Zaheer, M. Sanjabi, A. Talwalkar, and V. Smith. Federated optimization in heterogeneous networks. *Proceedings of Machine Learning and Systems*, 2:429–450, 2020.
- [24] W. Li and A. McCallum. Pachinko allocation: Dag-structured mixture models of topic correlations. In *International Conference on Machine learning*, pages 577–584, 2006.
- [25] X. Li, K. Huang, W. Yang, S. Wang, and Z. Zhang. On the convergence of fedavg on non-iid data. *arXiv preprint arXiv:1907.02189*, 2019.
- [26] X. Li, M. Jiang, X. Zhang, M. Kamp, and Q. Dou. Fed{bn}: Federated learning on non-{iid} features via local batch normalization. In *International Conference on Learning Representations*, 2021.
- [27] X. Lian, C. Zhang, H. Zhang, C.-J. Hsieh, W. Zhang, and J. Liu. Can decentralized algorithms outperform centralized algorithms? a case study for decentralized parallel stochastic gradient descent. *Advances in Neural Information Processing Systems*, 30, 2017.
- [28] B. McMahan, E. Moore, D. Ramage, S. Hampson, and B. A. y Arcas. Communication-efficient learning of deep networks from decentralized data. In *Artificial Intelligence and Statistics*, pages 1273–1282. PMLR, 2017.
- [29] B. T. Polyak and A. B. Juditsky. Acceleration of stochastic approximation by averaging. *SIAM Journal on Control and Optimization*, 30(4):838–855, 1992.
- [30] G. Pu, Y. Zhou, D. Wu, and X. Li. Server averaging for federated learning. *arXiv preprint arXiv:2103.11619*, 2021.
- [31] A. Rame, M. Kirchmeyer, T. Rahier, A. Rakotomamonjy, P. Gallinari, and M. Cord. Diverse weight averaging for out-of-distribution generalization. *arXiv preprint arXiv:2205.09739*, 2022.
- [32] S. J. Reddi, Z. Charles, M. Zaheer, Z. Garrett, K. Rush, J. Konečný, S. Kumar, and H. B. McMahan. Adaptive federated optimization. In *International Conference on Learning Representations*, 2021.

- [33] K. Simonyan and A. Zisserman. Very deep convolutional networks for large-scale image recognition. *arXiv preprint arXiv:1409.1556*, 2014.
- [34] I. Tenison, S. A. Sreeramadas, V. Mugunthan, E. Oyallon, E. Belilovsky, and I. Rish. Gradient masked averaging for federated learning. *arXiv preprint arXiv:2201.11986*, 2022.
- [35] J. Wang, Z. Charles, Z. Xu, G. Joshi, H. B. McMahan, M. Al-Shedivat, G. Andrew, S. Avestimehr, K. Daly, D. Data, et al. A field guide to federated optimization. *arXiv preprint arXiv:2107.06917*, 2021.
- [36] J. Wang, R. Das, G. Joshi, S. Kale, Z. Xu, and T. Zhang. On the unreasonable effectiveness of federated averaging with heterogeneous data. *arXiv preprint arXiv:2206.04723*, 2022.
- [37] J. Wang, Q. Liu, H. Liang, G. Joshi, and H. V. Poor. Tackling the objective inconsistency problem in heterogeneous federated optimization. *Advances in Neural Information Processing Systems*, 33:7611–7623, 2020.
- [38] H. Xiao, K. Rasul, and R. Vollgraf. Fashion-mnist: a novel image dataset for benchmarking machine learning algorithms. *arXiv preprint arXiv:1708.07747*, 2017.
- [39] N. Ye, K. Li, H. Bai, R. Yu, L. Hong, F. Zhou, Z. Li, and J. Zhu. Ood-bench: Quantifying and understanding two dimensions of out-of-distribution generalization. In *Proceedings of the IEEE/CVF Conference on Computer Vision and Pattern Recognition*, pages 7947–7958, 2022.
- [40] H. Yu, S. Yang, and S. Zhu. Parallel restarted sgd with faster convergence and less communication: Demystifying why model averaging works for deep learning. In *Proceedings of the AAAI Conference on Artificial Intelligence*, volume 33, pages 5693–5700, 2019.
- [41] M. Yurochkin, M. Agarwal, S. Ghosh, K. Greenewald, N. Hoang, and Y. Khazaeni. Bayesian nonparametric federated learning of neural networks. In *International Conference on Machine Learning*, pages 7252–7261. PMLR, 2019.
- [42] J. Zhang, C. De Sa, I. Mitliagkas, and C. Ré. Parallel sgd: When does averaging help? *arXiv preprint arXiv:1606.07365*, 2016.
- [43] Y. Zhao, M. Li, L. Lai, N. Suda, D. Civin, and V. Chandra. Federated learning with non-iid data. *arXiv preprint arXiv:1806.00582*, 2018.
- [44] T. Zhou, J. Zhang, and D. Tsang. Fedfa: Federated learning with feature anchors to align feature and classifier for heterogeneous data. *arXiv preprint arXiv:2211.09299*, 2022.
- [45] M. Zinkevich, M. Weimer, L. Li, and A. Smola. Parallelized stochastic gradient descent. *Advances in Neural Information Processing Systems*, 23, 2010.

Appendix

The Appendix is organized as follows.

- In Section A, we provide more loss and error landscape visualizations with different setups of FL to show the geometric properties of FMA.
- In Section B, we further analyze the variance term and covariance term of the expected error decomposition of FMA.
- In Section C, we describe our specific setups of all the experiments, including baseline setups, experiment setups and model setups.
- In Section D, we provide all the proof for the analysis in this work.

A Comprehensive loss/error landscape visualization of FL

According to [6, 11], the implementation of the loss/classification-error landscape visualization with three models is described as follows. We construct a plane that includes three model vectors $\mathbf{w}_1, \mathbf{w}_2, \mathbf{w}_3$ by two base vectors $\bar{\mathbf{u}} = \mathbf{u}/\|\mathbf{u}\|^2$ and $\bar{\mathbf{v}} = \mathbf{v}/\|\mathbf{v}\|^2$, where $\mathbf{u} = \mathbf{w}_2 - \mathbf{w}_1$ and $\mathbf{v} = (\mathbf{w}_3 - \mathbf{w}_1) - \langle \mathbf{w}_3 - \mathbf{w}_1, \mathbf{w}_2 - \mathbf{w}_1 \rangle / \|\mathbf{w}_2 - \mathbf{w}_1\|^2 \cdot (\mathbf{w}_2 - \mathbf{w}_1)$. Next, a point P with coordinates (x, y) in the plane represents a model $\mathbf{w}_P = \mathbf{w}_1 + x \cdot \bar{\mathbf{u}} + y \cdot \bar{\mathbf{v}}$. Finally, we evaluate the loss/classification-error of \mathbf{w}_P on a specific dataset and visualize the loss/error in this plane. Please note that the specific setups for all experiments in this section are provided in Table 6.

A.1 Loss landscape visualization of cross-device and cross-silo FL

We consider two FL setups: cross-device FL and cross-silo FL in this subsection, as described in [13]. In the case of cross-silo FL, a small number of clients is involved (e.g., the cross-silo FL shown in Figure 8 includes 10 clients), and all clients participate fully in each communication round. The cross-device FL require a large amount of clients, and only a subset of them participate in each round (e.g., the cross-device FL in Figure 8 involves 100 clients with 0.1 participation rate at each round). Figure 8 displays the loss landscape visualization with three models on the global dataset for both cross-device and cross-silo FL setups.

Similar to the FMA’s geometrical properties observed from Figure 1, both cross-device FL and cross-silo FL show that FMA model (i.e., the *white cross*) achieves lower test loss and error compared to the client models (i.e., the *black triangles*) throughout the training process. Furthermore, both FL setups illustrate that FMA keeps client models and global models closely located within a shared basin. Additionally, it is worth noting that the deviation between the *white cross* and the lowest point of the basin in terms of loss/error is smaller in comparison to the deviation observed in the cross-silo FL visualization shown in Figure 8. This finding supports the analysis presented in Section 4, which suggests that low participation rates amplify the deviation.

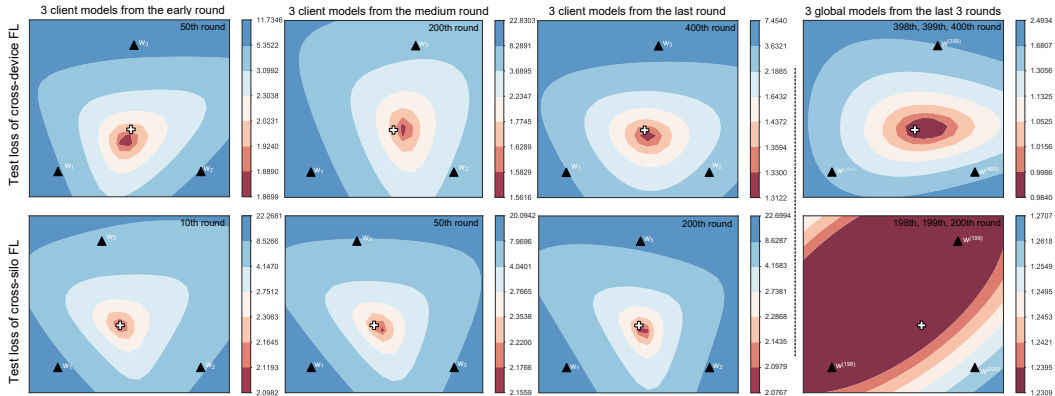


Figure 8: Loss landscape visualization with three models on global testset in cross-device and cross-silo FL.

In addition to the loss landscape, we also visualize the classification error landscape on the global dataset in cross-device and cross-silo FL setups in Figure 9. The observed geometric properties of FMA in Figure 9 are similar to those depicted in Figure 8. Therefore, we will not repeat the descriptions here.

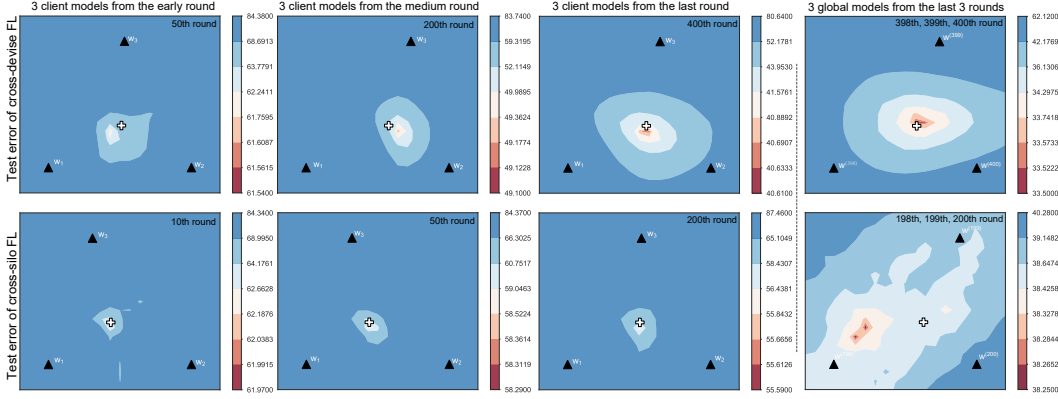


Figure 9: Error landscape visualization with three models on global testset in cross-device and cross-silo FL.

A.2 Loss landscape visualization of FL under different models, datasets and data heterogeneity

To further explore the geometrical properties of FMA, we visualize the loss landscape of FL under various models (including the CNN model and the ResNet model), datasets (including FMNIST and CIFAR-10) and data heterogeneity (including label skews with $\#C = 2$ and $\alpha = 0.1$). These visualizations are presented in Figure 10. The geometrical properties of FMA, as denoted in Section 2 are consistent to those obtained in Figure 10. Regardless of the specific FL setup, FMA ensures that client models and the global model reside within a common basin. This geometric insight sheds light on how FMA prevents client models from over-fitting on their respective datasets (i.e., FMA mitigates the over-fitting information of client models being aggregated into the global model) and improves its generalization on the global dataset.

B Further analysis of error decomposition

B.1 Further analysis on the variance term

For the analysis of the variance term, we set $n_i = n_j$ (i.e., the number of client samples is the same) in order to isolate the impact of weighted averaging on the error decomposition in Theorem 1.

Corollary 2. (Error decomposition of FMA with the same client sample sizes. Extended from Theorem 1.) Given K client models $\{\mathbf{w}_k\}_{k=1}^K \in \prod_k \mathcal{W}_{\mathcal{D}_k}$ and $n_i/n = n_j/n = 1/K$, we can decompose the expected error of the FMA's model \mathbf{w}_{FMA} on \mathcal{D} as:

$$\begin{aligned} \mathbb{E}_{\{\mathbf{w}_k\}_{k=1}^K} \mathcal{E}(\mathbf{w}_{\text{FMA}}) &= \frac{1}{nK^2} \sum_{(x,y) \in \mathcal{D}} \left[\sum_{k=1}^K \text{TrainBias}\{f_{\mathbf{w}_k}|(x,y)\} + \text{HeterBias}\{f_{\mathbf{w}_k}|(x,y)\} \right]^2 \\ &+ \frac{1}{K} \underbrace{\sum_{k=1}^K \frac{1}{K} \text{Var}\{f_{\mathbf{w}_k}|x\}}_{\overline{\text{Var}}\{f_{\mathbf{w}_k}\}_{k=1}^K|x} + \sum_k \frac{K-1}{K^2} \underbrace{\sum_{k' \neq k} \frac{1}{K-1} \text{Cov}\{f_{\mathbf{w}_k}, \mathbf{w}_{k'}|x\}}_{\overline{\text{Cov}}\{f_{\mathbf{w}_k}, \mathbf{w}_{k'}|x\}} + O(\Delta^2), \end{aligned} \quad (5)$$

where $\text{Var}\{f_{\mathbf{w}_k}|x\} = \mathbb{E}_{\mathbf{w}_k} [(f_{\mathbf{w}_k}(x) - \mathbb{E}_{\mathbf{w}_k}[f_{\mathbf{w}_k}(x)])^2]$; $\text{Cov}\{f_{\mathbf{w}_k}, \mathbf{w}_{k'}|x\} = \mathbb{E}_{\mathbf{w}_k, \mathbf{w}_{k'}} [(f_{\mathbf{w}_k}(x) - \mathbb{E}_{\mathbf{w}_k}[f_{\mathbf{w}_k}(x)])(f_{\mathbf{w}_{k'}}(x) - \mathbb{E}_{\mathbf{w}_{k'}}[f_{\mathbf{w}_{k'}}(x)])]$; $\overline{\text{Var}}\{f_{\mathbf{w}_k}\}_{k=1}^K|x$ denotes

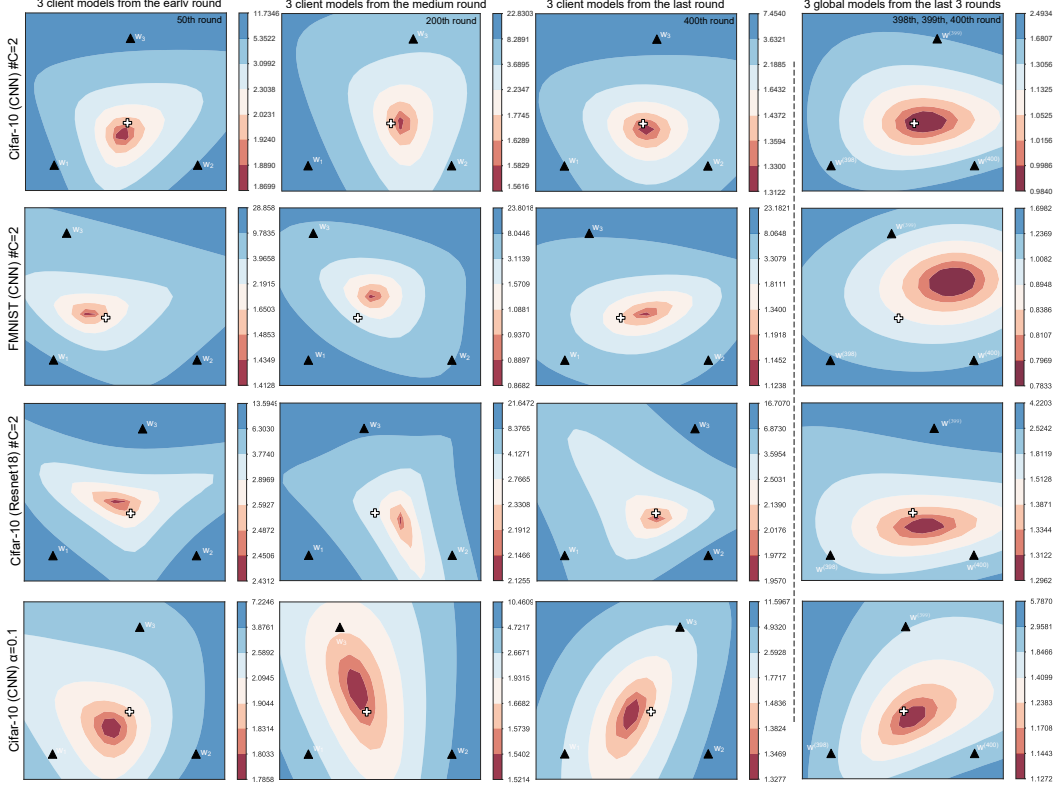


Figure 10: Loss landscape visualization of client and global models in FL under different setups. **First row** denotes the visualization of CNN models trained by FL under data heterogeneity $\#C = 2$ of CIFAR-10; **Second row** denotes the visualization of CNN models trained by FL under $\#C = 2$ on FMNIST; **Third row** denotes the visualization of Resnet18 trained by FL under $\#C = 2$ on CIFAR-10; **Fourth row** denotes the visualization of CNN models trained by FL when the Dirichlet parameter $\alpha = 0.1$ on CIFAR-10.

the mean prediction variance of client models when given a sample $(x, y) \in \mathcal{D}$; $\overline{\text{Cov}}\{f_{\mathbf{w}_k}, \mathbf{w}_{k'} | x\}$ denotes the mean prediction covariance between two client models when given a sample $(x, y) \in \mathcal{D}$.

From Theorem 1 in [39] and Proposition 2 in [31], we have the following property of the variance term:

Theorem 2. (Bounded variance. From [39, 31]) Given a kernel regime $f_{\mathbf{w}_k}$ trained on client dataset \mathcal{D}_k (of size n_k) with neural tangent kernel $K_{f_{\mathbf{w}_k}}$, when $\exists(\lambda_{\mathcal{D}_k}, \epsilon)$ with $0 \leq \epsilon \ll \lambda_{\mathcal{D}_k}$ such that $\forall x_i \in \mathcal{D}_k, K_{f_{\mathbf{w}_k}}(x_i, x_i) = \lambda_{\mathcal{D}_k}$ and $\forall x_i, x_j \in \mathcal{D}_k$ and $i \neq j, |K_f(x_i, x_j)| \leq \epsilon$, the variance on the global dataset \mathcal{D} is:

$$\mathbb{E}_{x \in \mathcal{D}}[\text{Var}\{f_{\mathbf{w}_k} | x\}] = \frac{n_k}{2\lambda_{\mathcal{D}_k}} \text{MMD}^2(\mathcal{D}_k, \mathcal{D}) + \lambda_{\mathcal{D}} - \frac{n_k}{2\lambda_{\mathcal{D}_k}} \beta_{\mathcal{D}} + O(\epsilon), \quad (6)$$

where $\text{MMD}(\cdot)$ is the empirical maximum mean discrepancy in the reproducing kernel Hilbert space (RKHS) of $K_{f_{\mathbf{w}_k}}(x_i, x_j)$; $\lambda_{\mathcal{D}} = \mathbb{E}_{x \in \mathcal{D}} K_{f_{\mathbf{w}_k}}(x, x)$ and $\beta_{\mathcal{D}} = \mathbb{E}_{x_i, x_j \in \mathcal{D}, i \neq j} K_{f_{\mathbf{w}_k}}^2(x_i, x_j)$ denote the empirical mean similarities of identical and different samples averaged over \mathcal{D} , respectively.

In Theorem 2, both $\lambda_{\mathcal{D}}$ and $\beta_{\mathcal{D}}$ are dependent solely on the global dataset \mathcal{D} when given $f_{\mathbf{w}_k}$. The global dataset \mathcal{D} represents the combination of all client datasets, and can be considered as a fixed dataset within FL. Consequently, $\lambda_{\mathcal{D}}$ and $\beta_{\mathcal{D}}$ can be regarded as constants that depend on \mathcal{D} in Theorem 2. Therefore, Theorem 2 demonstrates that the variance term in Theorem 1 is solely associated with $\text{MMD}^2(\mathcal{D}_k, \mathcal{D})$, which represents the distance between the client dataset \mathcal{D}_k and the global dataset \mathcal{D} in FL setups. By considering the fixed global dataset and its relationship with the client datasets, Theorem 2 highlights the significance of the distance measure $\text{MMD}(\cdot)$ in

quantifying the domain shift between client and global datasets, where $MMD(\cdot)$ can be computed with the L1 distance as with [39].

By combining Theorem 2 and Corollary 2, we can deduce that the mean prediction variance of client models, denoted as $\overline{\text{Var}}\{f_{\{\mathbf{w}_k\}_{k=1}^K}|x\}$ in Theorem 2, is constant when considering a sample $(x, y) \in \mathcal{D}$. Consequently, the variance term will diminish as the number of averaged client models increases. However, it is important to note that the impact of the client-model number becomes negligible when all client models are identically distributed (i.e., client models are trained on homogeneous datasets with the same training configures). This is due to the fact that the covariance term and the sum of the variance term (i.e., $\text{Var}\{f_{\mathbf{w}_k}|x\} = \text{Cov}\{f_{\mathbf{w}_k}, \mathbf{w}_{k'}|x\}$ when client models are identically distributed) in Theorem 2 are equal to the prediction variance of a single client model.

In summary, as the number of averaged client models increases, the variance term decreases. However, in the case of identically distributed client models (trained on homogeneous datasets), the influence of the client-model number on the variance term diminishes, and the variance term is essentially equivalent to the prediction variance of a single client model.

B.2 Further analysis on the covariance term

To analyze the covariance term, we consider $n_i = n_j, \forall i, j \in [K]$ (i.e., the number of client samples is the same) to ablate the impact of weighted averaging on the error decomposition in Theorem 1. Furthermore, we perform a decomposition of the covariance term in Theorem 1 and obtain the following result:

Corollary 3. (Lower bound of the covariance term.) For $n_i = n_j$ when $i \neq j$, the covariance term in Theorem 1 is bounded by:

$$\begin{aligned} \mathbb{E}_{(x,y) \in \mathcal{D}} \left(\frac{1}{K^2} \sum_k \sum_{k'} \text{Cov}\{f_{\mathbf{w}_k}, \mathbf{w}_{k'}|x\} \right) &= \frac{1}{nK^2} \sum_{(x,y) \in \mathcal{D}} \sum_k \sum_{k'} \text{Cov}\{f_{\mathbf{w}_k}, \mathbf{w}_{k'}|x\} \\ &\geq \frac{K-1}{nK} \sum_{(x,y) \in \mathcal{D}} \min_{(k,k')} \text{Cov}\{f_{\mathbf{w}_k}, \mathbf{w}_{k'}|x\} \end{aligned} \quad (7)$$

where $\min_{(k,k')} \text{Cov}\{f_{\mathbf{w}_k}, \mathbf{w}_{k'}|x\}$ measures the maximum discrepancy of the prediction error on \mathbf{w}_k and $\mathbf{w}_{k'}$.

The physical meaning of $\min_{(k,k')} \text{Cov}\{f_{\mathbf{w}_k}, \mathbf{w}_{k'}|x\}$, when given a sample $(x, y) \in \mathcal{D}$, can be understood as follows: Firstly, $\text{Cov}\{f_{\mathbf{w}_k}, \mathbf{w}_{k'}|x\}$ calculates the prediction covariance between client models \mathbf{w}_k and $\mathbf{w}_{k'}$. Then, $\min_{(k,k')} \text{Cov}\{f_{\mathbf{w}_k}, \mathbf{w}_{k'}|x\}$ find the minimal value of $\text{Cov}\{f_{\mathbf{w}_k}, \mathbf{w}_{k'}|x\}$ across all client pairs (k, k') where $\forall k, k' \in [K], k \neq k'$. Essentially, the minimal value measures the largest diversity among client models on the given sample (x, y) . The diversity is determined by the maximum discrepancy between client datasets \mathcal{D}_k and $\mathcal{D}_{k'}$ when the client models share the same training configurations, as discussed in [31]. Therefore, Corollary 3 demonstrates that the covariance term has a lower bound, which depends on the maximum discrepancy across client datasets. This lower bound can be considered as a constant if the client datasets remain unchanged during FL training. In other words, for FMA, increasing the diversity among client models may have little impact on reducing the error of the global model. This is because the diversity of client models is inherently large due to data heterogeneity, which is different from the benefit of model diversity in domain generalization, as discussed in [31].

C Experiment setups

C.1 Models

The models used in all the experiments, including validation, test, and ablation, are presented in Table 4. To isolate the controversial effect of BN layers on FL, we follow [10] to replace the BN layer with the GroupNorm layer in all experiments. For a fair comparison, our models adhere to the architectures reported in the baseline works. Specifically, for the experiments conducted on the FMNIST and CIFAR-10 datasets, we utilize a CNN model consisting of two 5x5 convolutional layers followed by 2x2 max pooling, as well as two fully-connected layers with ReLU activation. This architecture

aligns with the model used in [44]. For the CIFAR-10/100 experiments, we adopt the ResNet-18 architecture [9] with a linear projector. This choice is consistent with the models employed in [32] and [26]. Lastly, for the Digit Fives dataset, we employ a CNN model with three 5x5 convolutional layers followed by five GroupNorm layers.

Table 4: Parameter settings for all the models used in our experiments. Group normalization layers split input channels into two groups in all models.

Layer	Dataset					
	FMNIST CNN	CNN	CIFAR-10/100 VGG11	Resnet18	Digit Five CNN	PACS AlexNet
1	Conv2d(1,32,5) ReLU,MaxPool2D(2,2)	Conv2d(3,64,5) ReLU,MaxPool2D(2,2)	Basicbone of VGG11 with GN	Basicbone of Resnet18 with GN	Conv2d(3,64,5,1,2) GN(2,64) ReLU,MaxPool2D(2,2)	Basicbone of AlexNet with GN
2	Conv2d(1,32,5) ReLU,MaxPool2D(2,2)	Conv2d(64,64,5) ReLU,MaxPool2D(2,2)	VGG11.FC(512,128)	Resnet18.FC(512,128)	Conv2d(64,64,5,1,2) GN(2,64) ReLU,MaxPool2D(2,2)	Resnet18.FC(4096,512)
3	FC(512,384) ReLU	FC(1600,384) ReLU	FC(128,10)	FC(128,10)	Conv2d(64,128,5,1,2) GN(2,128) ReLU,MaxPool2D(2,2)	FC(512,10)
4	FC(384,128)	FC(384,128)			FC(6272, 2048) ReLU	
5	FC(128,10)	FC(128,10)			FC(2048,128)	
6					FC(128,10)	

C.2 Baseline setups

Table 5 provides the additional hyper-parameters specific to different baselines. These hyper-parameters are chosen based on the the setups of hyper-parameters reported in the respective baseline works. Here is a brief description of the role of hyper-parameters in each baseline:

- FedProx and FedFA: These baselines modify the loss function by adding a proximal term at the client side. The best coefficient of the proximal term is selected from the given range [0.1, 0.01, 0.001]. This coefficient controls the trade-off between the proximal loss function and the main loss function.
- FedASAM: This baseline utilizes the Sharpness-Aware Minimization (SAM) technique as the client loss function. The hyper-parameters η_{SAM} and ρ_{SAM} control the noise introduced in SAM, affecting the exploration-exploitation trade-off during optimization.
- FedAdam and FedYogi: These baselines introduce adaptive momentum on the global update at the server side. Hyper-parameters include the server learning rate (lr) η , decay parameters β_1, β_2 and the degree of adaptivity τ_1 . These hyper-parameters control the adaptation of the server-side optimizer’s momentum over time.
- FedGMA: This baseline applies the AND-Masked gradient update based on the masking threshold ϵ . The masking threshold determines the level of sparsity in the gradient updates and improve the flatness of the global model.

It is worth noting that FedAvg and FedNova do not require additional hyper-parameters beyond the standard optimization parameters.

Table 5: Hyper-parameter setups for all the baselines. FedAvg and FedNova are not be involved as they do not require additional hyper-parameters.

Hyper-parameter	FedProx (+IMA)	FedASAM (+IMA)	FedFA (+IMA)	FedAdam (+IMA)	FedYogi (+IMA)	FedGMA (+IMA)
	coefficient of proximal term: Best from [0.1, 0.01,0.001]	CNN models: $\rho_{\text{SAM}}=0.7$, $\eta_{\text{SAM}}=0.2$ Other models: $\rho_{\text{SAM}}=0.2$, $\eta_{\text{SAM}}=0.05$	coefficient of proximal term: Best from [0.1, 0.01,0.001] coefficient of anchor updates: 0.9	$\eta = 0.01$	$\beta_1 = 0.9$ $\beta_2 = 0.99$ $\tau_1 = 0.001$	$\eta = 0.0001$ $\epsilon = 0.8$
Refer	-	Authors’ codes	Appendix in [44]: the same experiments	Benchmark:Flower	Reproduces codes	

C.3 Setup of all visualization and validation experiments

Table 6 provides the specific setups for all visualization and validation experiments. The experiments are performed using PyTorch on a single node of the High-Performance Computing platform. The

node is equipped with 4 NVIDIA A30 Tensor Core GPUs, each with 24GB of memory. The setups include various parameters and configurations specific to each experiment, such as the model architecture, dataset, number of clients, batch size, learning rate, optimizer, and other relevant details.

Table 6: Setup of all visualization and validation experiments in this work. $\#C = 2$ implies that each client holds two class shardings of training dataset, where each sharding consists of 250 samples. $\alpha = 0.1$ represents to split training dataset with Dirichlet distribution $Dir(\alpha) = 0.1$ as [41].

	FL	client number	client sampling	local epoch	local batch	lr (momentum)	lr decay per round	round	dataset	heterogeneous data(C:class)	model
Figure 1, 9	Cross-device FL	100	0.1	5	50	0.01(0.9)	0	400	CIFAR-10	$\#C = 2$	CNN
Figure 8, 9	Cross-silo FL	10	1	5	50	0.01(0.9)	0	200	CIFAR-10	$\#C = 2$	CNN
Figure 10	Cross-device FL	100	0.1	5	50	0.01(0.9)	0	400	CIFAR-10	$\#C = 2, \alpha = 0.1$	CNN, Resnet18
Figure 2, 3, 4	Cross-silo FL	10	1	5	50	0.01(0.9)	0/0.01	400	CIFAR-10	$\#C = 2$	CNN
Figure 5	Cross-device FL	100	0.1	5	50	0.01(0.9)	0	400	CIFAR-10	$\#C = 2$	CNN

C.4 Setup of test experiments

Table 7 provides the setup details for all test experiments conducted in this work. The table includes information such as the client number, participation rate, local epoch number, lr, decay scheme, total communication rounds, model, and specific setups of IMA. Please refer to Table 7 for a comprehensive overview of the experimental configurations.

Table 7: Setup of all test experiments in Table 1.

Table 1	client number	participation rate	local epoch	local batch	lr (momentum)	lr decay per round	round	windows size	IMA lr decay	start IMA(0.75)	Model
FMNIST	100	0.1	5	50	0.01(0.9)	0.01	300	5	0.03	225	CNN
CIFAR-10	100	0.1	5	50	0.01(0.9)	0.01	400	5	0.03	300	CNN, Resnet18
CIFAR-100	100	0.1	5	50	0.01(0.9)	0.01	300,400	5	0.03	225,300	VGG11, Resnet18
Digit Five	100	0.1	5	50	0.01(0.9)	0.01	200	5	0.03	150	CNN w/ GN
PACS	80	0.2	5	50	0.01(0.9)	0.01	400	5	0.03	300	AlexNet w/ GN

D Proof

D.1 Proof of Lemma 1

Suppose that clients would not hold an extremely unbalanced dataset (i.e., $n_i/n_j \neq \infty$ when $i \neq j$).

Proof. (Proof of Lemma 1) For client k and the FMA’s model, we have:

$$f_{\mathbf{w}_k}(x) = f_{\mathbf{w}_{\text{FMA}}}(x) + \langle \Delta f_{\mathbf{w}_{\text{FMA}}}(x), \Delta_k \rangle + O(\|\Delta_k\|^2), \quad (8)$$

where $\langle \cdot, \cdot \rangle$ is the dot product, and $\Delta_k = \mathbf{w}_k - \mathbf{w}_{\text{FMA}}$. Thus, we build the relationship between the FMA-model function and the WENS function as:

$$\begin{aligned} f_{\text{WENS}}(x) &= \sum_{k=1}^K \frac{n_k}{n} f_{\mathbf{w}_k}(x) = f_{\mathbf{w}_{\text{FMA}}}(x) + \sum_{k=1}^K \frac{n_k}{n} \langle \Delta f_{\mathbf{w}_{\text{FMA}}}(x), \Delta_k \rangle + \sum_{k=1}^K \frac{n_k}{n} O(\|\Delta_k\|^2) \\ &= f_{\mathbf{w}_{\text{FMA}}}(x) + \left\langle \Delta f_{\mathbf{w}_{\text{FMA}}}(x), \sum_{k=1}^K \frac{n_k}{n} \Delta_k \right\rangle + O(\|\Delta\|^2) \\ &= f_{\mathbf{w}_{\text{FMA}}}(x) + O(\|\Delta\|^2), \end{aligned} \quad (9)$$

where $\|\Delta\| = \max_k^K \|\Delta_k\|$, $n = \sum_k n_k$ is the total sample number. \square

D.2 Proof of Theorem 1

Proof. (Proof of Theorem 1) Substituting $f_{\text{WENS}}(x) = \sum_{k=1}^K \frac{n_k}{n} f_{\mathbf{w}_k}$ into (1), we have:

$$\mathbb{E}_{\{\mathbf{w}_k\}_{k=1}^K \in \prod_k^K \mathcal{W}_{\mathcal{D}_k}} \mathcal{E}(\{\mathbf{w}_k\}_{k=1}^K) = \mathbb{E}_{(x,y) \in \mathcal{D}} [(\text{Bias}\{f_{\text{WENS}}|(x,y)\})^2 + \text{Var}\{f_{\text{WENS}}|x\}]. \quad (10)$$

For the bias term, we have:

$$\begin{aligned}
\text{Bias}\{f_{\text{WENS}}|(x, y)\} &= y - \mathbb{E}_{\{\mathbf{w}_k\}_{k=1}^K} f_{\text{WENS}}(x) = y - \mathbb{E}_{\{\mathbf{w}_k\}_{k=1}^K} \left[\sum_{k=1}^K \frac{n_k}{n} f_{\mathbf{w}_k}(x) \right] \\
&= y - \sum_{k=1}^K \frac{n_k}{n} \mathbb{E}_{\mathbf{w}_k} [f_{\mathbf{w}_k}(x)] \\
&= \sum_{k=1}^K \frac{n_k}{n} (y - \mathbb{E}_{\mathbf{w}_k} [f_{\mathbf{w}_k}(x)])
\end{aligned} \tag{11}$$

Taking the expectation of the bias term with respect to the global dataset, we have:

$$\begin{aligned}
\mathbb{E}_{(x,y) \in \mathcal{D}} (\text{Bias}\{f_{\text{WENS}}|(x, y)\})^2 &= \frac{1}{n} \sum_{(x,y) \in \mathcal{D}} \left[\sum_{k=1}^K \frac{n_k}{n} \underbrace{\mathbb{I}[(x, y) \in \mathcal{D}_k] (y - \mathbb{E}_{\mathbf{w}_k} [f_{\mathbf{w}_k}(x)])}_{\text{TrainBias}\{f_{\mathbf{w}_k}|(x,y)\}} \right. \\
&\quad \left. + \sum_{k=1}^K \frac{n_k}{n} \underbrace{\mathbb{I}[(x, y) \in \mathcal{D} \setminus \mathcal{D}_k] (y - \mathbb{E}_{\mathbf{w}_k} [f_{\mathbf{w}_k}(x)])}_{\text{HeterBias}\{f_{\mathbf{w}_k}|(x,y)\}} \right]^2.
\end{aligned} \tag{12}$$

For the variance term, we have:

$$\begin{aligned}
\text{Var}\{f_{\text{WENS}}|(x, y)\} &= \mathbb{E}_{\{\mathbf{w}_k\}_{k=1}^K} \left[\left(\sum_{k=1}^K \frac{n_k}{n} f_{\mathbf{w}_k}(x) - \mathbb{E}_{\{\mathbf{w}_k\}_{k=1}^K} \left[\sum_{k=1}^K \frac{n_k}{n} f_{\mathbf{w}_k}(x) \right] \right)^2 \right] \\
&= \sum_{k=1}^K \frac{n_k^2}{n^2} \underbrace{\mathbb{E}_{\mathbf{w}_k} \left[(f_{\mathbf{w}_k}(x) - \mathbb{E}_{\mathbf{w}_k} [f_{\mathbf{w}_k}(x)])^2 \right]}_{\text{Var}\{f_{\mathbf{w}_k}|x\}} \\
&\quad + \sum_k \sum_{k' \neq k} \frac{n_k n_{k'}}{n^2} \underbrace{\mathbb{E}_{\mathbf{w}_k, \mathbf{w}_{k'}} \left[(f_{\mathbf{w}_k}(x) - \mathbb{E}_{\mathbf{w}_k} [f_{\mathbf{w}_k}(x)]) (f_{\mathbf{w}_{k'}}(x) - \mathbb{E}_{\mathbf{w}_{k'}} [f_{\mathbf{w}_{k'}}(x)]) \right]}_{\text{Cov}\{f_{\mathbf{w}_k, \mathbf{w}_{k'}}|x\}}.
\end{aligned} \tag{13}$$

Taking the expectation of the variance term with respect to the global dataset, we have:

$$\begin{aligned}
\mathbb{E}_{(x,y) \in \mathcal{D}} (\text{Var}\{f_{\text{WENS}}|(x, y)\}) &= \mathbb{E}_{(x,y) \in \mathcal{D}} \left(\sum_{k=1}^K \frac{n_k^2}{n^2} \text{Var}\{f_{\mathbf{w}_k}|x\} + \sum_k \sum_{k'} \frac{n_k n_{k'}}{n^2} \text{Cov}\{f_{\mathbf{w}_k, \mathbf{w}_{k'}}|x\} \right) \\
&= \frac{1}{n} \sum_{(x,y) \in \mathcal{D}} \sum_{k=1}^K \frac{n_k^2}{n^2} \text{Var}\{f_{\mathbf{w}_k}|x\} + \frac{1}{n} \sum_{(x,y) \in \mathcal{D}} \sum_k \sum_{k'} \frac{n_k n_{k'}}{n^2} \text{Cov}\{f_{\mathbf{w}_k, \mathbf{w}_{k'}}|x\}.
\end{aligned} \tag{14}$$

Using the Taylor expansion at the zeroth order of the loss, we extend Lemma 1 and obtain:

$$\begin{aligned}
\mathcal{E}(\mathbf{w}_{\text{FMA}}) &= \mathbb{E}_{(x,y) \in \mathcal{D}} [l(f_{\mathbf{w}_{\text{FMA}}}(x); y)] \\
&= \mathbb{E}_{(x,y) \in \mathcal{D}} [l(f_{\text{WENS}}(x); y)] + O(\|f_{\mathbf{w}_{\text{FMA}}}(x) - f_{\text{WENS}}(x)\|_2) \\
&= \mathcal{E}(\{\mathbf{w}_k\}_{k=1}^K) + O(\Delta^2).
\end{aligned} \tag{15}$$

Finally, combining (12) and (14) with (10), we have:

$$\begin{aligned}
\mathbb{E}_{\{\mathbf{w}_k\}_{k=1}^K \in \prod_k \mathcal{W}_{\mathcal{D}_k}} \mathcal{E}(\mathbf{w}_{\text{FMA}}) &= \mathbb{E}_{\{\mathbf{w}_k\}_{k=1}^K \in \prod_k \mathcal{W}_{\mathcal{D}_k}} \mathcal{E}(\{\mathbf{w}_k\}_{k=1}^K) + O(\Delta^2) \\
&= \mathbb{E}_{(x,y) \in \mathcal{D}} \left[(\text{Bias}\{f_{\text{WENS}}|(x, y)\})^2 + \text{Var}\{f_{\text{WENS}}|x\} \right] + O(\Delta^2) \\
&= \frac{1}{n} \sum_{(x,y) \in \mathcal{D}} \left[\sum_{k=1}^K \frac{n_k}{n} \text{TrainBias}\{f_{\mathbf{w}_k}|(x, y)\} + \frac{n_k}{n} \text{HeterBias}\{f_{\mathbf{w}_k}|(x, y)\} \right]^2 \\
&\quad + \sum_{k=1}^K \frac{n_k^2}{n^2} \text{Var}\{f_{\mathbf{w}_k}|x\} + \sum_k \sum_{k'} \frac{n_k n_{k'}}{n^2} \text{Cov}\{f_{\mathbf{w}_k, \mathbf{w}_{k'}}|x\} \\
&\quad + O(\Delta^2).
\end{aligned} \tag{16}$$

□

D.3 Proof of Corollary 1

We make the assumption that $\text{TrainBias}\{f_{\mathbf{w}_i}|(x, y)\} = 0$, which is practical since $\text{TrainBias}\{f_{\mathbf{w}_i}|(x, y)\}$ in Theorem 1 is almost close to 0, as verified in Figure 2. Under this assumption, given a client dataset \mathcal{D}_i with the maximum discrepancy to the global dataset \mathcal{D} , $\text{HeterBias}\{f_{\mathbf{w}_i}|(x, y)\} \geq \text{HeterBias}\{f_{\mathbf{w}_j}|(x, y)\}$ when $i \neq j$ according to Theorem 1, and $\text{Var}\{f_{\mathbf{w}_j}|x\} \geq \text{Var}\{f_{\mathbf{w}_i}|x\}$ when $i \neq j$ according to Theorem 2. In other words, the client model \mathbf{w}_i trained on its dataset \mathcal{D}_i has the largest error when tested on the global dataset \mathcal{D}_i (i.e., $i = \arg \max_i \mathbb{E}_{\mathbf{w}_i \in \mathcal{W}_{\mathcal{D}_i}} \mathcal{E}(\mathbf{w}_i)$).

Proof. (Proof of Corollary 1) We can decompose the expected error of the client model \mathbf{w}_i on \mathcal{D} according to [5] as:

$$\begin{aligned} \mathbb{E}_{\mathbf{w}_i} \mathcal{E}(\mathbf{w}_i) &= \frac{1}{n} \sum_{(x, y) \in \mathcal{D}} [\text{TrainBias}\{f_{\mathbf{w}_i}|(x, y)\} + \text{HeterBias}\{f_{\mathbf{w}_i}|(x, y)\}]^2 + \text{Var}\{f_{\mathbf{w}_i}|x\} \\ &= \frac{1}{n} \sum_{(x, y) \in \mathcal{D}} \left[\sum_k^K \frac{n_k}{n} \text{HeterBias}\{f_{\mathbf{w}_i}|(x, y)\} \right]^2 + \frac{1}{n} \sum_{(x, y) \in \mathcal{D}} \sum_k^K \frac{n_k}{n} \text{Var}\{f_{\mathbf{w}_i}|x\}. \end{aligned} \quad (17)$$

According to Theorem 1, we have:

$$\begin{aligned} \mathbb{E}_{\{\mathbf{w}_k\}_{k=1}^K \in \prod_k^K \mathcal{W}_{\mathcal{D}_k}} \mathcal{E}(\mathbf{w}_{\text{FMA}}) &= \frac{1}{n} \sum_{(x, y) \in \mathcal{D}} \left[\sum_k^K \frac{n_k}{n} \text{HeterBias}\{f_{\mathbf{w}_k}|(x, y)\} \right]^2 \\ &+ \frac{1}{n} \sum_{(x, y) \in \mathcal{D}} \left[\sum_{k=1}^K \frac{n_k^2}{n^2} \text{Var}\{f_{\mathbf{w}_k}|x\} + \sum_k \sum_{k' \neq k} \frac{n_k n_{k'}}{n^2} \text{Cov}\{f_{\mathbf{w}_k, \mathbf{w}_{k'}}|x\} \right] + O(\Delta^2). \end{aligned} \quad (18)$$

The difference between $\mathbb{E}_{\{\mathbf{w}_k\}_{k=1}^K \in \prod_k^K \mathcal{W}_{\mathcal{D}_k}} \mathcal{E}(\mathbf{w}_{\text{FMA}})$ and $\mathbb{E}_{\mathbf{w}_i} \mathcal{E}(\mathbf{w}_i)$ can be computed as:

$$\begin{aligned} \mathbb{E}_{\{\mathbf{w}_k\}_{k=1}^K \in \prod_k^K \mathcal{W}_{\mathcal{D}_k}} \mathcal{E}(\mathbf{w}_{\text{FMA}}) - \mathbb{E}_{\mathbf{w}_i} \mathcal{E}(\mathbf{w}_i) &\leq \frac{1}{n} \sum_{(x, y) \in \mathcal{D}} \sum_k^K \left(\frac{n_k^2}{n^2} \text{Var}\{f_{\mathbf{w}_k}|x\} - \frac{n_k}{n} \text{Var}\{f_{\mathbf{w}_i}|x\} \right) \\ &+ \frac{1}{n} \sum_{(x, y) \in \mathcal{D}} \sum_k \sum_{k' \neq k} \frac{n_k n_{k'}}{n^2} \text{Cov}\{f_{\mathbf{w}_k, \mathbf{w}_{k'}}|x\} + O(\Delta^2) \\ &\leq \frac{1}{n} \sum_{(x, y) \in \mathcal{D}} \sum_k^K \left(\frac{n_k^2 - n n_k}{n^2} \text{Var}\{f_{\mathbf{w}_i}|x\} \right) + \frac{1}{n} \sum_{(x, y) \in \mathcal{D}} \sum_k \sum_{k' \neq k} \frac{n_k n_{k'}}{n^2} \text{Cov}\{f_{\mathbf{w}_k, \mathbf{w}_{k'}}|x\} + O(\Delta^2) \\ &\leq \frac{1}{n} \sum_{(x, y) \in \mathcal{D}} \sum_k^K \left(\frac{n_k^2 - n n_k}{n^2} \text{Var}\{f_{\mathbf{w}_i}|x\} \right) + \frac{1}{n} \sum_{(x, y) \in \mathcal{D}} \sum_k^K \frac{n_k n - n_k^2}{n^2} \text{Cov}\{f_{\mathbf{w}_i, \mathbf{w}_i}|x\} + O(\Delta^2) \\ &= \frac{1}{n} \sum_{(x, y) \in \mathcal{D}} \sum_k^K \frac{n_k n - n_k^2}{n^2} (\text{Cov}\{f_{\mathbf{w}_i, \mathbf{w}_i}|x\} - \text{Var}\{f_{\mathbf{w}_i}|x\}) + O(\Delta^2) \\ &= O(\Delta^2) \end{aligned} \quad (19)$$

where the first inequality holds because $\text{HeterBias}\{f_{\mathbf{w}_i}|(x, y)\} \geq \text{HeterBias}\{f_{\mathbf{w}_k}|(x, y)\}$ when $i \neq k$, the second inequality follows $\text{Var}\{f_{\mathbf{w}_i}|x\} \geq \text{Var}\{f_{\mathbf{w}_k}|x\}$ when $i \neq k$, the third inequality follows $\text{Cov}\{f_{\mathbf{w}_i, \mathbf{w}_i}|x\} = \text{Var}\{f_{\mathbf{w}_i}|x\} \geq \text{Var}\{f_{\mathbf{w}_k}|x\} = \text{Cov}\{f_{\mathbf{w}_k, \mathbf{w}_k}|x\} \geq \text{Cov}\{f_{\mathbf{w}_k, \mathbf{w}_{k'}}|x\}$ when $k \neq k'$ and $\mathbf{w}_k, \mathbf{w}_{k'}$ are trained on heterogeneous data, and the last equality holds because $\text{Cov}\{f_{\mathbf{w}_i, \mathbf{w}_i}|x\} = \text{Var}\{f_{\mathbf{w}_i}|x\}$.

Finally, we obtain $\mathbb{E}_{\{\mathbf{w}_k\}_{k=1}^K \in \prod_k^K \mathcal{W}_{\mathcal{D}_k}} \mathcal{E}(\mathbf{w}_{\text{FMA}}) - \mathbb{E}_{\mathbf{w}_i} \mathcal{E}(\mathbf{w}_i) \leq O(\Delta^2)$. This indicates that under the locality constraint, the expected error of the global model is smaller than that of the client model whose client dataset has the maximum discrepancy to the global dataset. □